Classification of Carbide Distributions using Scale Selection and Directional Distributions*

Klaus Wiltschi[1], *Tony Lindeberg*[2] *and Axel Pinz*[1]

[1]Institute for Computer Graphics and Vision, TU-Graz, Austria.
Email: {wiltschi, pinz}@icg.tu-graz.ac.at, http://www.icg.tu-graz.ac.at

[2]Computational Vision and Active Perception Laboratory,
KTH, S-100 44, Stockholm, Sweden.
Email: tony@nada.kth.se, http://www.nada.kth/~tony

Technical Report ISRN KTH/NA/P–97/10–SE
Shortened version in Proc. Int. Conf. on Image Processing (ICIP'97),
Santa Barbara, California, October 26–29, 1997

Abstract

In the production of high speed steel, the rolling affects the micro-structure of the steel, which in turn influences the mechanical properties. Specifically, the distribution of carbide is essential, since cracks propagate within the carbide agglomerations. In current quality control, the properties of the steel are assessed manually by comparison with a standard chart, containing representative patterns for each steel class.

Interestingly, the standard technique for classifying carbide distributions is two-dimensional, where the first dimension basically corresponds to *scale* ("degree" — the size of the largest carbide agglomeration) and the the second dimension basically reflects the *directional distribution* ("type" — how strongly the net structure of carbide has been stretched).

In this paper, we present an automatic method for such classification based on scale-space operations, in which the size information is measured using recently developed techniques for feature detection with automatic scale selection and the directional information is computed from second-moment descriptors (Lindeberg 1994). Combined with a morphological verification scheme, a pattern classifier is proposed, which shares large similarities with current manual techniques.

Compared to previous work (Wiltschi, Pinz & Hackl 1995), the proposed scheme has the advantage that the significant scale of the carbide agglomeration is calculated explicitly, and the method is much less sensitive to the variance of spatial connectivity than a morphological approach.

From a theoretical viewpoint, the proposed scheme also has the attractive property that it is based on similar visual-front-end operations as a large class of computer vision modules.

Keywords: scale, scale-space, scale selection, feature detection, second moment matrix, carbide classification, high speed steel.

*The work performed by the ICG was supported by a grant from the Böhler Edelstahl GmbH (BEG), Kapfenberg (Austria)

Contents

1 Introduction

The classification of carbide distributions is an important task in the quality control of high speed steel. Currently, specially skilled metallographers classify the carbide distributions (at a magnification of 100:1) using a light microscope and assigning them to a standard chart of 28 images, arranged in 4 rows and 7 columns as shown in Figure 1.

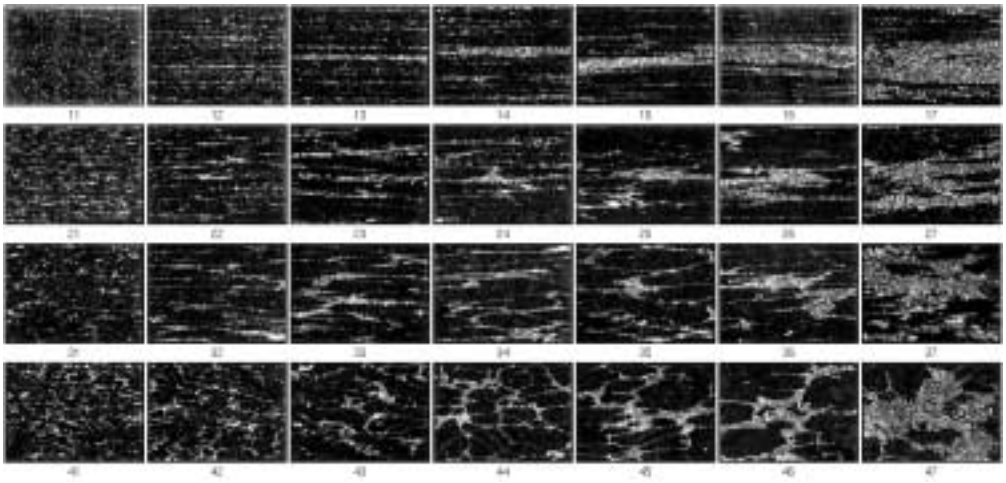

Figure 1: The microscopic standard chart for characterizing carbide distributions of high speed steels. The first number of the class (the row index) denotes the *type* of the distribution, which corresponds to the *shape* of the agglomerations. The second number (the column index) describes the *degree*, basically reflecting the *size* of the agglomerations. (The carbide particles are white in all images.)

This standard chart distinguishes carbide distributions according to visually captured features, referred to as the 'size' and 'shape' of the (white) carbide agglomerations. In each row, the 'size' of the agglomerations increases from left to right (the *degree* of the distribution), whereas in each column the 'shape' ranges from band-shaped to net-shaped structures from top to bottom (the *type* of the distribution), caused by the stretching of originally net-shaped structures during the rolling process. In this respect, the standard chart can be interpreted as categorizing the carbide distributions into 4×7 classes according to the 'shape' and the 'size' of the carbide agglomerations.

The subject of this article is to present a method which performs this classification automatically based on recently developed computer vision tools for feature detection with automatic scale selection (Lindeberg 1994, Lindeberg 1996*b*, Lindeberg 1996*a*) combined with texture descriptors derived from second moment descriptors (Bigün, Granlund & Wiklund 1991, Lindeberg 1994, Gårding & Lindeberg 1996). The image descriptors obtained in this way will then be verified by a morphological scheme (Wiltschi 1995, Wiltschi et al. 1995). Compared to this previous work, it will be shown that the robustness of the classification is improved by the inclusion of grey-level based image descriptors and explicit handling of the scale information based on scale-space operations.

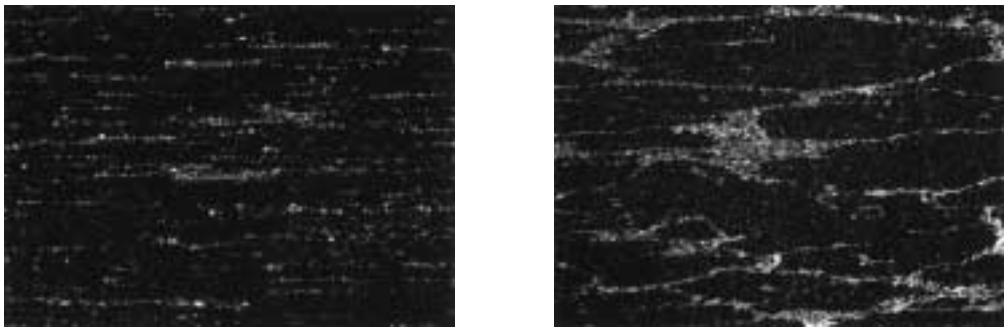

(a) Reference image 22 with dominant small band-like carbide agglomerations.

(b) Reference image 35, containing dominant large net-like structures.

Figure 2: Enlargements of two images from the standard chart; carbides are white.

2 Scale selection module

To handle the inherent multi-scale nature of image data, the notion of scale-space theory (Witkin 1983, Koenderink 1984, Lindeberg 1990, Florack, ter Haar Romeny, Koenderink & Viergever 1992, Lindeberg 1994) has been developed by the computer vision community. For any N-dimensional image $f: \mathbb{R}^N \to \mathbb{R}$, its *scale-space representation* $L : \mathbb{R}^N \times \mathbb{R}_+ \to \mathbb{R}$ is defined by

$$L(\cdot;\ t) = g(\cdot;\ t) * f(\cdot) \tag{1}$$

where $g : \mathbb{R}^N \times \mathbb{R}_+ \to \mathbb{R}$ denotes the N-dimensional Gaussian kernel:

$$g(\cdot;\ t) = \frac{1}{(2\pi t)^{N/2}} e^{\frac{-(x_1^2+\cdots+x_N^2)}{2t}} \tag{2}$$

and the variance $t \in R^+$ of the Gaussian kernel is referred to as the *scale parameter*. Based on this representation, *scale space derivatives* are defined by

$$L_{x^\alpha}(\cdot;\ t) = \partial_{x_1^{\alpha_1} \cdots x_N^{\alpha_N}} L(\cdot;\ t) = (\partial_{x_1^{\alpha_1} \cdots x_N^{\alpha_N}} g(\cdot;\ t)) * f(\cdot) \tag{3}$$

with corresponding *normalized derivatives* given by

$$\partial_{\xi_i^n} = t^{n/2}\, \partial_{x_i^n} \tag{4}$$

where ξ represents the normalized coordinate corresponding to the variable x and n denotes the order of differentiation.

In terms of this framework, a large number of feature detectors can be formulated as (linear and non-linear) combinations of partial derivatives. Specifically, scale levels for feature detection can be selected by detecting local extrema over scales of such differential geometric descriptors (Lindeberg 1993, Lindeberg 1994, Lindeberg 1996*b*, Lindeberg 1996*a*).

2.1 Detection and ranking of significant image structures

In the manual classification procedure, the "size" of the largest agglomerations in each image constitutes a primary cue. Since the agglomerations mainly form blob- or ridge-like structures (see Figure 2 for two examples), we have decided to use a *ridge detector*, which builds upon the earlier methods for ridge detection described in (Haralick 1983, Eberly, Gardner, Morse, Pizer & Scharlach 1994, Koenderink & van Doorn 1994, Pizer, Burbeck, Coggins, Fritsch & Morse 1994) and is defined as follows (Lindeberg 1996*a*):

Introduce a local (p, q)-coordinate system at each image point, defined by the mixed second-order derivative being zero (*i.e.*, $L_{pq} = 0$). Then, we can detect (possibly elongated, bright) blob features from points which are simultaneously maximal with respect to space and scales in

$$-L_{pp,norm} = -t\, L_{pp} \tag{5}$$

where L_{pp} is the principal curvature having the largest absolute value.

To rank these features on significance, we multiply the normalized response $L_{pp,norm}$ at each scale-space maximum by a factor of $\sqrt{t}$, which gives the following *significance measure*[1] $S(A)$ for each scale-space extremum

$$S(A) = -\sqrt{t}\, L_{pp,norm}(x, y). \tag{6}$$

Figure 3(a) shows the result of applying this operation to one of the reference images in the chart (image 33).

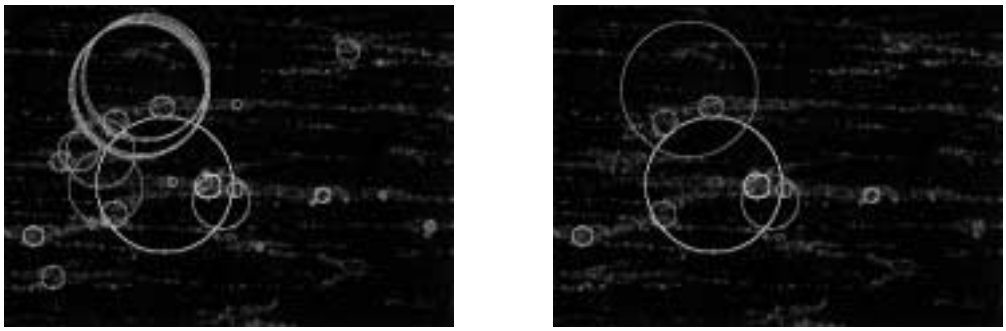

(a) The 30 most significant responses.

(b) The 10 strongest responses after overlap suppression.

Figure 3: The most significant ridge features detected from (5) and (6). Each response is illustrated by a circle with the radius proportional to the selected scale. The intensity of the circles are also coded such that brighter values indicate more significant features.

As can be seen from the example, certain image structures give rise to multiple responses. To suppress overlapping features, any scale-space maximum A is rejected if there exists any scale-space extremum B such that

[1] An intuitive motivation for this weighting is that the width of the ridge feature can be expected to be proportional to $\sqrt{t}$.

$$\begin{array}{c} \text{center}(A) \in \text{support region}(B) \ \wedge \\ \text{center}(B) \in \text{support region}(A) \ \wedge \\ t_A/t_B \in \left[\frac{1}{\alpha}, \alpha\right]; \qquad \alpha > 1 \\ S(A) < S(B) \end{array} \tag{7}$$

where we have chosen $\alpha = 4$, corresponding to a ratio of 2 between the blob radii.

2.2 Verification of detected image features

To suppress spurious responses from the feature detection module ("false alarms"), we use the following verification mechanism, which constitutes an extension of a previously developed morphological module for perceptual grouping of substructures (Wiltschi et al. 1995, Wiltschi 1995):

1. An elliptical support region is associated with each detected scale-space maximum based on the two principal curvatures $L_{pp,norm}/L_{qq,norm}$ as well as the orientation of the ridge. Starting from an idealized two-dimensional elliptical blob model defined by

$$g(x, y;\ t_1, t_2) = \frac{1}{\sqrt{2\pi t_1}} e^{\frac{-x^2}{2t_1}} \frac{1}{\sqrt{2\pi t_2}} e^{\frac{-y^2}{2t_2}}, \tag{8}$$

   the ratio t_2/t_1 between the major and the minor axis of the ellipse can be estimated as (see Appendix A.2 for a derivation; (Lindeberg 1996*a*))

$$\frac{t_2}{t_1} = \frac{1}{2}\left(3\ \frac{L_{pp,norm}}{L_{qq,norm}} - 1\right), \tag{9}$$

   where an upper bound of $t_2/t_1 \leq 2$ is used to prevent overestimation of the support region.

Within each such support region the following verification scheme is applied:

2. A binary mask of the *characteristic structure* in the image is generated using previously developed segmentation algorithm (Wiltschi et al. 1995). This processing step essentially corresponds to adaptive thresholding followed by morphological opening and closing yielding a binary image showing connected components for the carbide agglomerations (see Figure 4(b)).

3. By determining the area of these components, *the characteristic structure* is defined to contain only agglomerations with an area larger than 10% of the area of the largest agglomeration in this image

   After this operation, the largest non-overlapping circular opposite regions in the support region are computed from a Euclidean distance map (Fig. 4(c)) in which local extrema are detected (Fig. 4(d)).

(a) Elliptical support region (10 most significant extrema).

(b) Binary mask with characteristic structure.

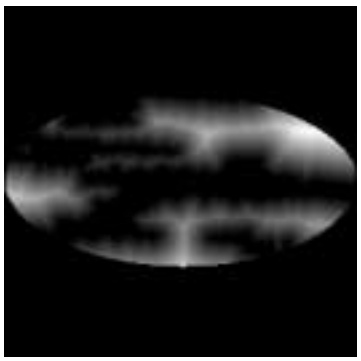

(c) Euclidean distance map within support of large scale extremum.

(d) Local extrema in distance map.

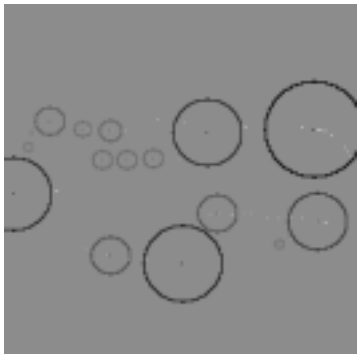

(e) Non-overlapping largest opposite circular regions.

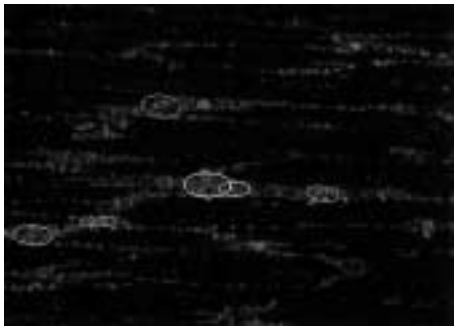

(f) Verified structures (10 most significant extrema).

Figure 4: Verification of the most significant entities using elliptical support regions, in which the largest non-overlapping circular opposite regions of the *characteristic structure* are determined. (This is reference image 33; and in all images brighter means higher significance.)

4. Then, the sizes A_i of these opposite regions are used for suppressing feature responses with interfering substructures. This suppression is performed by multiplying the significance measure by

$$W = \left(\frac{C}{C + \frac{A_{opposite}}{A_{support}}} \right)^m , \tag{10}$$

where the area $A_{support}$ of the characteristic structure is related to a measure $A_{opposite}$ of the areas of all n largest blobs of opposite polarity contained in the elliptic support region (Fig. 4(e))

$$A_{opposite} = \sum_{i=1}^{n} A_i \tag{11}$$

and $C = 0.5$ and $m = 2$ are constants. The parameter values occurring here were chosen to maximize the classification performance of the resulting size description feature R_{detect} according to the *degree* of the carbide distribution (see section 4).

Figure 4(f) shows the most significant structures after this verification step (and thus the composed verification procedure).

5. Finally, after the transformation (10) of the significance values, the k most significant extrema are selected, and the radius R_{detect} of the largest extremum is used as a size description feature for the classification of the carbide distribution according to the *degree*, i.e.

$$R_{detect} = \sqrt{2\, t_{detect}\, \log 2}; \qquad t_{detect} = \max(t_1, \ldots, t_k) \tag{12}$$

where $k = 10$.

This size descriptor is illustrated in Figure 5, where the largest detected structures are marked (the length of the minor axes of the ellipse is equal to R_{detect}) for two neighboring reference images in two different rows.

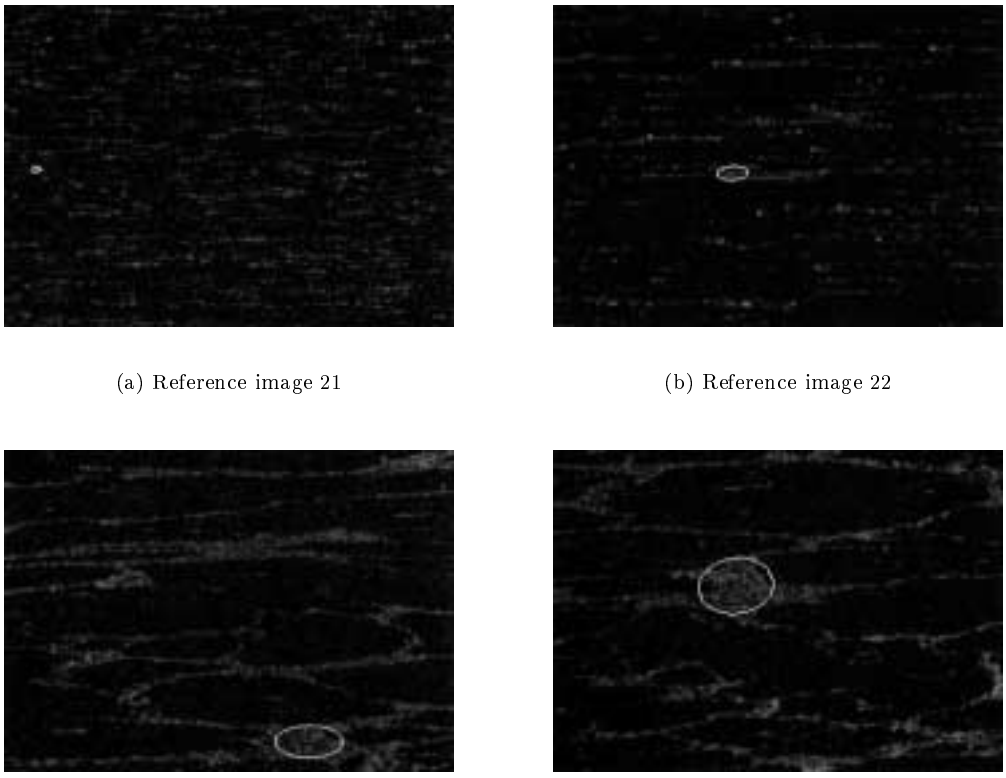

(a) Reference image 21

(b) Reference image 22

(c) Reference image 34

(d) Reference image 35

Figure 5: The largest structures obtained by applying composed detection/verification procedure to two neighboring rows and columns in the reference chart.

3 Shape estimation

3.1 The multi-scale windowed second moment matrix

To represent directional distributions, the second moment matrix is a useful texture descriptor (Bigün et al. 1991, Gårding & Lindeberg 1996, Lindeberg & Gårding 1993). Given a symmetric normalized window function w, the *windowed second moment matrix* can be defined by

$$\mu_L(q) = \int_{x \in \mathbb{R}^2} (\nabla L(x))(\nabla L(x))^T w(q-x)dx, \tag{13}$$

where $L : \mathbb{R}^2 \to \mathbb{R}$ denotes the image brightness and $\nabla L = (L_x, L_y)^T$ its gradient. Denoting the windowing operation by E_q, Equation (13) can be written as

$$\mu_L(q) = \begin{pmatrix} \mu_{11} & \mu_{12} \\ \mu_{21} & \mu_{22} \end{pmatrix} = E_q \begin{pmatrix} L_x^2 & L_x L_y \\ L_x L_y & L_y^2 \end{pmatrix} = E_q((\nabla L)(\nabla L)^T) \tag{14}$$

and from the components of μ_L, the following descriptors can be defined

$$P = E_q(L_x^2 + L_y^2), \quad C = E_q(L_x^2 - L_y^2), \quad S = 2E_q(L_x L_y). \tag{15}$$

Here, P is a measure for the strength of the operator response, whereas C and S contains directional information, which can be summarized in two anisotropy measures

$$Q = \sqrt{C^2 + S^2}, \qquad \tilde{Q} = Q/P. \tag{16}$$

The *normalized anisotropy* $\tilde{Q} \in [0;1]$ is zero, if and only if $E_q(L_x^2) = E_q(L_y^2)$ and $E_q(L_x L_y) = 0$ and $\tilde{Q} = 1$ if and only if $E_q(L_x L_y) = E_q(L_x^2)E_q(L_y^2)$. A rotationally symmetric gray-level pattern has $\tilde{Q} = 0$ and a translationally symmetric pattern has $\tilde{Q} = 1$.

When computing this descriptor in practice, the gradient vectors are defined at *local scale* t_l and we use a Gaussian window function g with *integration scale* t_i (Lindeberg 1994, chap. 14). Therefore, the *multi-scale windowed second moment matrix* μ_L is defined as

$$\mu_L(q; t_l, t_i) = \int_{x \in \mathbb{R}^2} (\nabla L(x))(\nabla L(x))^T g(q-x; t_i)dx. \tag{17}$$

3.2 Scale selection for computing anisotropy

In the manual classification procedure, the directional distribution of the carbide agglomerations is evaluated to estimate the "shape" (*type*) of the carbide distribution. This estimation can be modeled by evaluating the *multi-scale second moment matrix* $\mu_L(q; t_l, t_i)$ based on the scale information of the scale selection scheme described in section 2. Therefore, the normalized anisotropy $\tilde{Q}$ is calculated for

$$t_l = \gamma_l * t_{detect}, \tag{18}$$

where the parameter value $\gamma_l = 0.5$ has been chosen to maximize the classification performance of the shape descriptor $\tilde{Q}$ according to the *type* (see section 4).

Under the assumption that the image has a globally valid significant scale[2] for computing shape descriptors of the carbide distribution, the integration scale is set to the size of the image. In other words, global values of P, C and S are computed by summing up the corresponding gradient expressions over the whole image and determining global values of Q and $\tilde{Q}$ afterwards. This yields a shape description feature for classifying carbide distributions according to their *type* (see section 4):

$$\tilde{Q}_{detect} = \tilde{Q}(\mu_L(x, y;\ t_l, image\ size)) \tag{19}$$

4 Classification results

To evaluate the size and shape descriptors obtained from the composed feature detection scheme, we evaluated the methodology on a reference data base consisting of 429 images, in which each sample has been classified independently by 4 metallographers. For each sample, the most frequent classification was used as the 'true' class. In this data, all four classifications agreed on 33% of the data, three of them in 39% of the cases, and two of them in remaining 28% of the data. This dataset was then split up into a training set of 290 carbide distributions and a disjunct test set with 139 images. The performance of the image features extracted from the data was evaluated by a minimum distance classifier.

To assess the performance of the size descriptor R_{detect} governing the determination of the *degree* (size) of the carbide distribution, all images of the same *degree* were combined into one class, yielding 7 degree classes. In a similar manner, we produced 4 type classes to evaluate the performance of the shape feature $\tilde{Q}_{detect}$ determining the *type* (shape) of the carbide distribution. Due to the non-quantitative definition of the standard chart, the in-class variances will be increased by this combination, which in turn decreases the performance of the classifier.

The classification rates of the resulting minimum distance classifiers for the *degree* and the *type*, respectively, are shown in table 1. Here, the value in the right column shows the percentage of images classified to the correct or to a directly neighboring class (i.e. allowing a one step class deviation, which is also common in the visual classification from the metallographers). [3]

Figure 6 shows the mean and standard deviation of the features for the whole sample set of 429 images versus the *degree* and *type*. The large variance in the values of $\tilde{Q}_{detect}$ for type 1 is mainly due to fact that almost no anisotropic (band-, or line-like) structures occur in the very fine-scale carbide structures (see fig. 1), which results in a low anisotropy value, as for the net-shaped structures. This drawback of low discrimination for the lowest degrees

[2] A detailed investigation of using local anisotropy measures computed using different scaling relations between the detected image features and the integration as well as local scales showed that in terms of successful classification rates, the global anisotropy measure outperforms local anisotropy over a reasonable range of size variations.

[3] If the data set used for training and evaluating the classifier is narrowed down to include only samples for which at least three of the metallographers agree on the same classification, then the performance of *degree* classifier increases to about 60% correctly classified samples.

	correct [%]	one class deviation [%]
R_{detect} (*degree*)	50	93
$\tilde{Q}_{detect}$ (*type*)	45	80

Table 1: Minimum distance classification performance according to the *degree* (using R_{detect}) and to the *type* (using $\tilde{Q}_{detect}$), respectively (percentage of correct classifications and one class deviation)

will be eliminated by including selected features from previous work (Wiltschi et al. 1995).

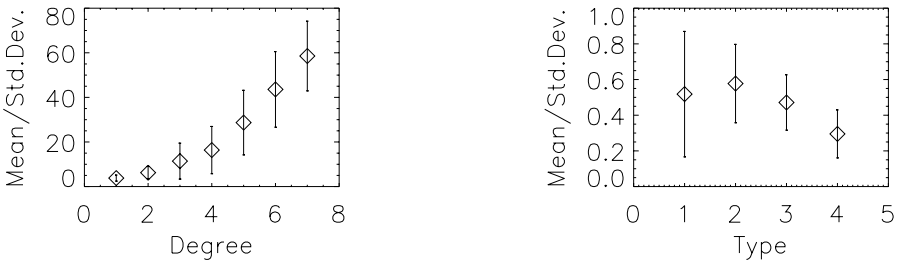

(a) size feature R_{detect}

(b) shape feature $\tilde{Q}_{detect}$

Figure 6: Mean and standard deviation of features in 7 *degree* and 4 *type* classes, respectively.

5 Conclusions

We have presented a characterization of carbide distributions, based on a scale selection mechanism, which leads to an intuitively reasonable result, and which is at the same time gives precise estimates of the visually captured 'size' and 'shape' information.

The 'size' (*degree*) of the carbide distribution is estimated by detecting significant blobs and ridges, using a scale selection scheme based on normalized derivatives in linear scale-space. The structures so detected, are then verified within an elliptical support region, by evaluating the *characteristic structure*, which is generated by a previously developed morphological segmentation scheme. After this set of processing steps, the scale of the largest significant and verified structure is used as a measure of the *degree* of the carbide distributions.

Then, the 'shape' (*type*) of the carbide distribution is estimated by a scale-tuned local texture descriptor, the *multi-scale windowed second moment matrix*, tuned by the scale information extracted in the first step. The evaluation of the anisotropy calculated from this directional information gives a measure of the *type* of the carbide distribution.

In our future work, the size and shape description features obtained from

the proposed scheme will be combined with a set of features derived from the earlier mentioned characteristic structure of the carbide distributions (Wiltschi et al. 1995) and be used as input to a feature selection algorithm, such as those reported by (Devijver & Kittler 1982, Pudil, Novovicová & Kittler 1994). Furthermore, the composed classification procedure will be integrated with the active inspection system described in (Wiltschi & Pinz 1996).

A Appendix

A.1 Radius of the half peak support region of circular blobs

The half peak support region of an idealized blob

$$g(x, y;\ t) = \frac{1}{2\pi t} e^{\frac{(x^2+y^2)}{2t}} \tag{20}$$

is given by a circle of radius

$$R = \sqrt{2t\ \log 2}. \tag{21}$$

A.2 Estimation of the elliptical blob support region

Based on an idealized elliptical blob model

$$g(x, y;\ t_1, t_2) = \frac{1}{\sqrt{2\pi t_1}} e^{\frac{x^2}{2t_1}} \frac{1}{\sqrt{2\pi t_2}} e^{\frac{y^2}{2t_2}} \tag{22}$$

for $t_1 < t_2$, the ratio of the principal curvature

$$\frac{L_{pp,norm}}{L_{qq,norm}} = \frac{t + t_2}{t + t_1} \tag{23}$$

and with the scale $t_{extremum}$, at which the local extremum over scale occurs,

$$t_{extremum} = \frac{1}{4}(t_1 - t_2) \pm \sqrt{\frac{1}{16}(t_1 - t_2)^2 + t_1 t_2} \tag{24}$$

the ratio of the axes of the elliptical blob can be estimated by

$$\frac{t_2}{t_1} = \frac{1}{2}\left(3\frac{L_{pp,norm}}{L_{qq,norm}} - 1\right), \tag{25}$$

where for an extremum detected at scale t_{detect} we used

$$t_1 := t_{detect}. \tag{26}$$

A.3 Scale selection results for the standard chart

For the images of the standard chart the 10 most significant extrema after the complete verification procedure are shown in figure 7. Furthermore, the size feature R_{detect} is illustrated by the largest most significant extremum for the reference images in figure 8.

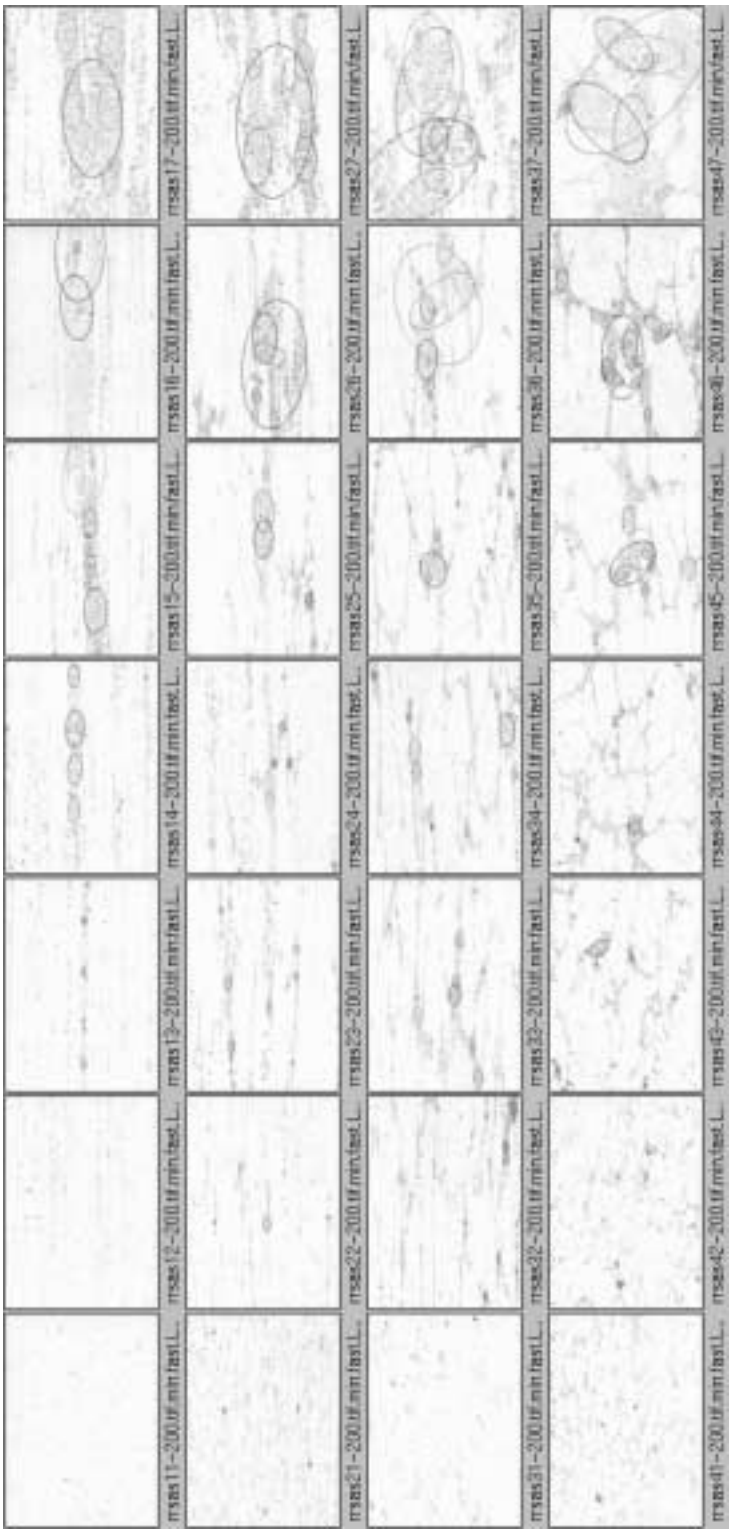

Figure 7: The 10 most significant extrema for the images in the reference chart (after completing the verification stage).

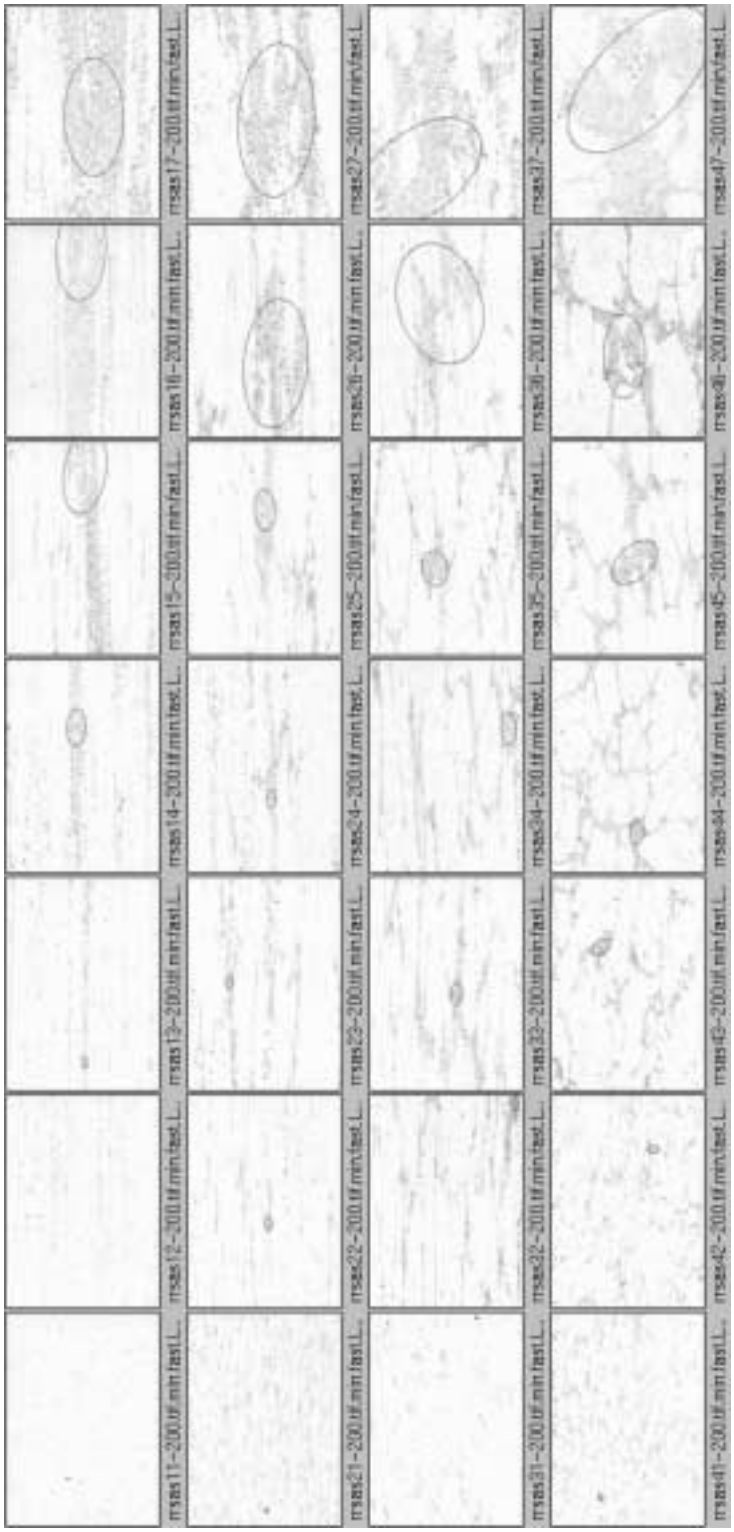

Figure 8: The most significant extremum extracted from each image in the reference chart.

References

Bigün, J., Granlund, G. H. & Wiklund, J. (1991), 'Multidimensional orientation estimation with applications to texture analysis and optical flow', *IEEE Transactions on Pattern Analysis and Machine Intelligence* **13**(8), 775–790.

Devijver, P. A. & Kittler, J. (1982), *Pattern Recognition: A statistical approach*, Pretice/Hall International.

Eberly, D., Gardner, R., Morse, B., Pizer, S. & Scharlach, C. (1994), 'Ridges for image analysis', *Journal of Mathematical Imaging and Vision* **4**(4), 353–373.

Florack, L. M. J., ter Haar Romeny, B. M., Koenderink, J. J. & Viergever, M. A. (1992), 'Scale and the differential structure of images', *Image and Vision Computing* **10**(6), 376–388.

Gårding, J. & Lindeberg, T. (1996), 'Direct computation of shape cues using scale-adapted spatial derivative operators', *International Journal of Computer Vision* **17**(2), 163–191.

Haralick, R. M. (1983), 'Ridges and valleys in digital images', *Computer Vision, Graphics, and Image Processing* **22**, 28–38.

Koenderink, J. J. (1984), 'The structure of images', *Biol. Cybern.* **50**, 363–370.

Koenderink, J. J. & van Doorn, A. J. (1994), 'Two-plus-one-dimensional differential geometry', *Pattern Recognition Letters* **15**(5), 439–444.

Lindeberg, T. (1990), 'Scale-space for discrete signals', *IEEE Transactions on Pattern Analysis and Machine Intelligence* **12**(3), 234–254.

Lindeberg, T. (1993), On scale selection for differential operators, *in* K. A. Hogdra, B. Braathen & K. Heia, eds, 'Proc. 8th Scandinavian Conference on Image Analysis', Norwegian Society for Image Processing and Pattern Recognition, Norway, pp. 857–866.

Lindeberg, T. (1994), *Scale-Space Theory in Computer Vision*, Kluwer Academic Publishers.

Lindeberg, T. (1996*a*), Edge detection and ridge detection with automatic scale selection, *in* 'Proc. CVPR'96', San Francisco, California, pp. 465–470.

Lindeberg, T. (1996*b*), Feature detection with automatic scale selection, Technical Report ISRN KTH/NA/P-96/18-SE, Dept. of Numerical Analysis, KTH. (to appear in IJCV).

Lindeberg, T. & Gårding, J. (1993), Shape from texture from a multi-scale perspective, *in* H.-H. Nagel, ed., 'Proc. 4th Int. Conf. on Computer Vision', Berlin, Germany, pp. 683–691.

Pizer, S. M., Burbeck, C. A., Coggins, J. M., Fritsch, D. S. & Morse, B. S. (1994), 'Object shape before boundary shape: Scale-space medial axis', *Journal of Mathematical Imaging and Vision* **4**, 303–313.

Pudil, P., Novovicová, J. & Kittler, J. (1994), 'Floating search methods in feature selection', *Pattern Recognition Letters* **15**, 1119–1125.

Wiltschi, K. (1995), Automatische Merkmalsextraktion aus Karbidverteilungsbildern von Schnellarbeitsstählen, Master's thesis, TU Graz.

Wiltschi, K. & Pinz, A. (1996), An active inspection system for the assessment of steel quality, *in* W. P. A. Pinz, ed., 'Machine Perception Applications - Proceedings of the IAPR-TC8 Workshop on Machine Perception Applications', Vol. 93, R. Oldenburg Wien Muenchen, pp. 127–136.

Wiltschi, K., Pinz, A. & Hackl, G. (1995), Feature extraction for carbide classification of high speed steel, *in* F. Solina & W. G. Kropatsch, eds, 'Proceedings of 19th ÖAGM and 1st SDVR Workshop - Visual Modules', Vol. 81, Österreichische Computer Gesellschaft, R. Oldenburg Wien München, pp. 169–176.

Witkin, A. P. (1983), Scale-space filtering, *in* 'Proc. 8th Int. Joint Conf. Art. Intell.', Karlsruhe, West Germany, pp. 1019–1022.